Satellite Measurements Reveal Persistent Small-Scale Features in Ocean Winds

Dudley B. Chelton,[1]* Michael G. Schlax,[1] Michael H. Freilich,[1] Ralph F. Milliff[2]

Four-year averages of 25-kilometer-resolution measurements of near-surface wind speed and direction over the global ocean from the QuikSCAT satellite radar scatterometer reveal the existence of surprisingly persistent small-scale features in the dynamically and thermodynamically important curl and divergence of the wind stress. Air-sea interaction over sea surface temperature fronts throughout the world ocean is evident in both the curl and divergence fields, as are the influences of islands and coastal mountains. Ocean currents such as the Gulf Stream generate distinctive patterns in the curl field. These previously unresolved features have important implications for oceanographic and air-sea interaction research.

The stress of the wind on the sea surface forces upper-ocean currents in a nonintuitive manner. Except near the equator, where the Coriolis acceleration from Earth's rotation vanishes, ocean currents are dominated by a balance between the pressure gradient force and the Coriolis acceleration. A consequence of this quasi-geostrophic balance is that ocean velocity is very nearly horizontally nondivergent. The ageostrophic motion by which the ocean adjusts to wind forcing is governed by the conservation of angular momentum, which implies that ocean circulation is forced primarily by the curl of the wind stress rather than by the wind stress itself (*1*).

Above the marine atmospheric boundary layer (MABL), which is generally confined to within about 1000 m of the sea surface, the wind field is also nearly geostrophic and nondivergent. Within the MABL, however, horizontal divergence (positive or negative, the latter corresponding to convergence) can develop and generate vertical motion in the lower atmosphere (*1*). Although wind stress divergence has little effect on ocean currents, it is an unambiguous indicator of air-sea interaction in regions of strong sea surface temperature (SST) gradients (*2*–*4*). The air-sea heat fluxes that give rise to divergence in the MABL tend to reduce the SST gradients (*5*).

Because of the paucity of direct observations over vast areas of the world ocean, air-sea interaction and ocean circulation modeling studies have relied primarily on wind estimates from coarse-resolution numerical weather prediction (NWP) models. Although the computational grids of global NWP models presently have a spacing of about 50 km, these models only resolve features in the surface wind field with spatial scales longer than about 500 km (*6*). Since July 1999, the QuikSCAT satellite scatterometer has provided spatially extensive wind measurements with more than an order of magnitude higher resolution than is presently obtainable from NWP models, and with much greater spatial and temporal coverage than that obtained from in situ observations or any previous scatterometer missions (*7*). The small-scale features in the wind field summarized here from the QuikSCAT measurements cannot be resolved by any other means.

Radar scatterometry. The SeaWinds scatterometer on the QuikSCAT satellite is a microwave radar launched and operated by the U.S. National Aeronautics and Space Administration (NASA). From 25-km measurements across a 1600-km swath, QuikSCAT samples more than 90% of the global ocean every 24 hours. Although the QuikSCAT coverage is impressive, the rapid evolution of weather systems in most regions of the world ocean can severely contaminate wind fields constructed from QuikSCAT data with insufficient temporal averaging (*8*). Such contamination is negligible in the 4-year averages considered here.

In all but rainy conditions, scatterometers infer the surface wind speed and direction at a given location from radar backscatter measurements of sea surface roughness obtained at multiple azimuths as the satellite moves along its orbit. Scatterometer wind retrievals are accurate to better than 2 m s^{-1} in speed and 20° in direction, which is essentially equivalent to the accuracy of in situ point measurements from buoys (*9*). Wind stress is readily estimated from the QuikSCAT vector wind retrievals (*10*).

To maximize spatial resolution, the wind stress curl and divergence were calculated from the QuikSCAT observations within each measurement swath and averaged on a global ¼° grid over the 4-year period from August 1999 to July 2003 (*11*). This swath-by-swath averaging of the curl and divergence at the maximum resolution of the QuikSCAT data is crucial to resolving many of the small-scale features discussed here (*12*), revealing previously unknown structures in the time-averaged wind stress field.

Large-scale features. In the 4-year average wind stress divergence field (top panels of Fig. 1 and fig. S1), the well-known Intertropical Convergence Zone (ITCZ) is evident across most of the Pacific between about 5°N and 10°N, where the northeast and southeast trade winds converge (*13*). Weaker ITCZs span the Atlantic and Indian Oceans. Elsewhere, the wind stress field is essentially nondivergent on large scales.

In contrast, there is significant large-scale wind stress curl throughout much of the world ocean (bottom panels of Fig. 1 and fig. S1). Latitudinal shears between the easterly trade winds, the midlatitude westerlies, and the polar easterlies result in large-scale curl patterns that are generally well represented in NWP models (Fig. 2 and fig. S4). These curls drive the large-scale ocean gyres and their associated intense western boundary currents (*1*).

Narrow bands of cyclonic curl (positive and negative in the Northern and Southern Hemispheres, respectively) with large alongshore scales adjacent to the western coastlines of continents play an important role in the dynamics of oceanic poleward countercurrents and undercurrents along these boundaries (*14*). The detailed structures and evolutions of these nearshore curl features are poorly resolved by historical ship observations (*15*) and are inaccurately represented in global NWP models (*16*).

The small-scale structures in the curl field that are of primary interest here are obscured in many regions by the large-scale patterns. Spatial high-pass filtering to remove features with wavelengths longer than 30° of longitude and 10° of latitude exposes a wealth of persistent small-scale features (Fig. 3 and fig. S2). Because the large-scale wind field is nearly nondivergent (except for the ITCZ), this filtering has little effect on the wind stress divergence (fig. S2).

[1]College of Oceanic and Atmospheric Sciences, 104 Ocean Administration Building, Oregon State University, Corvallis OR 97331–5503, USA. [2]Colorado Research Associates Division, Northwest Research Associates, 3380 Mitchell Lane, Boulder, CO 80301, USA.

It is evident from Fig. 3 and fig. S2 that many of the small-scale features in the curl are coincident geographically with regions of small-scale variability in the divergence. The causes of these features, which are much weaker or nonexistent in divergence and curl fields computed from NWP model winds (fig. S3), are discussed in the following sections.

SST effects. Much of the small-scale variability in the wind stress field is attributable to SST modification of low-level winds through the influence of air-sea heat flux on the MABL (fig. S5). Cool water stabilizes the MABL and decouples the surface winds from winds aloft. Heating over warm water deepens and destabilizes the MABL, decreasing the vertical shear of the wind (*5*, *17*–*23*). Differential heating of the MABL on opposite sides of an SST front also tends to create a pressure gradient force in the direction of the SST gradient (*24*, *25*). The net effects of SST on the MABL are to decrease the surface wind speed over cool water and increase it over warm water. Decelerations and accelerations as winds blow across SST fronts (fig. S6) lead respectively to surface wind convergences and divergences that are linearly related to the downwind component of the SST gradient (Fig. 4, top) (*3*, *4*).

Although it is a clear indicator of the influence of SST on low-level winds, the wind stress divergence cannot be easily quantified from in situ observations, because it requires simultaneous measurements over a large area. Previous scatterometer studies have identified this phenomenon regionally (*2*–*4*, *21*, *22*). The global divergence fields in the top panels of Fig. 1 and figs. S1 and S2 reveal the ubiquity, intensity, and surprising persistence of ocean-atmosphere coupling throughout the world ocean in regions of strong and persistent SST gradients. Bands of divergence just north of the equator in the Pacific and Atlantic occur where the southeast trade winds blow across the SST fronts on the north sides of equatorial cold tongues (*2*, *3*, *21*). Striations in the divergence over the western Arabian Sea are associated with monsoon winds blowing across the SST patterns of the well-known Great Whirl off the coast of Somalia and two persistent ocean eddies to the east (*26*).

Outside of the tropics, SST influence on the 4-year average wind stress is mostly restricted to regions poleward of 40° latitude, where persistent SST fronts are prevalent. Most striking are the alternating patches of divergence and convergence throughout the Southern Ocean poleward of 40°S, a region characterized by bathymetrically induced steady meanders of the Antarctic Circumpolar Current (ACC). These divergence and convergence patterns result from accelerations and decelerations of the mean westerly winds as they blow across SST fronts (*4*).

In the western North Atlantic, the mean northwesterly winds blow across the Gulf Stream east of Cape Hatteras (Fig. 5, bottom right). Acceleration toward the warmer water of the Gulf Stream and subsequent deceleration over the cooler water of the Sargasso Sea result in divergence over the inshore waters and convergence seaward of the Gulf Stream (top panels of Fig. 1 and figs. S1 and S2). Strong divergence occurs east of Newfoundland, where the westerly winds blow across the warm Gulf Stream after it turns northward around the Grand Banks. Similar structures associated with the Kuroshio Current can be seen in the northwest Pacific (*27*).

SST gradients also influence the wind stress curl. The filamentous structures in the curl field across most of the Southern Ocean (Fig. 3 and fig. S2) are manifestations of lateral gradients of air-sea interaction that occur where the westerly winds blow parallel to isotherms (fig. S6) associated with steady meanders of the ACC (*4*). Similar features are found wherever there are strong and persistent SST gradients, as in the eastern equatorial Pacific (*3*) and Atlantic and over the Sohm Plain and Newfoundland Basin in the northwest Atlantic. Throughout the world ocean, these small-scale features in the curl are linearly related to the crosswind SST gradient (Fig. 4, bottom) (*3*, *4*).

Orographic effects. Numerous examples of divergence and convergence related to orographic influences are visible in the top panels of Fig. 1 and figs. S1 and S2. Wind shadows form in the lee of many islands. Constriction of winds through mountain passes and interisland gaps and around the tips of many islands result in the formation of wind jets. These features are also evident in the curl fields (Fig. 3 and fig. S2). The clearest examples are found along the Pacific coast of Central America, where intense winds blow episodically from the Gulf of Mexico and Caribbean Sea through low-level moun-

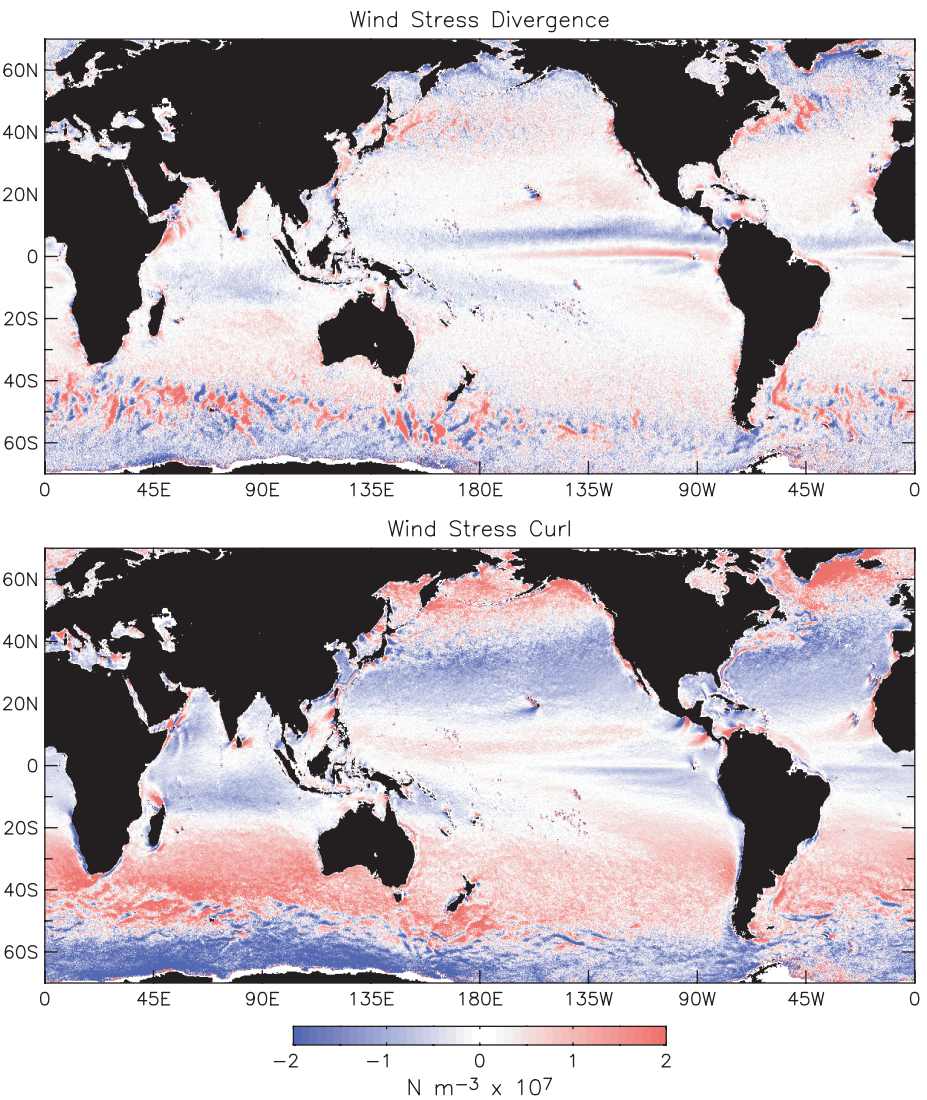

Fig. 1. Global 4-year averages (August 1999–July 2003) of the divergence (top) and curl (bottom) of the surface wind stress over the world ocean computed from 25-km-resolution wind measurements by the QuikSCAT scatterometer. (See fig. S1 for an electronic version of this figure.)

tain passes into the eastern Pacific (*28*). Viewed in the direction of the wind, the curl is positive and negative along the left and right sides of the jets, respectively (Fig. 5, top left). Wind-induced mixing and upwelling associated with these jets exert profound influences on the regional upper ocean circulation (*29*) and biology (*30*) and generate tongues of cold water that extend more than 500 km offshore (Fig. 5, bottom left).

Smaller wind jets are apparent in the Sea of Japan near Vladivostok (*31*), the Gulf of Lion in the Mediterranean Sea (the Mistral) (*32*), the lee of Cook Strait between the North and South Islands of New Zealand, and numerous other coastal locations near gaps in mountain topography.

Wind jets are also found in association with island wind shadows and corner accelerations. A spectacular corner acceleration is evident from the positive curl in the lee of Cape Farewell at the southern tip of Greenland (*33*). Upwelling associated with this curl, which can be underestimated by more than a factor of 2 in NWP models, preconditions the upper ocean for deep-water formation during wintertime cold-air outbreaks (*34*). Although the intense storms that are responsible for this strong 4-year average curl are intermittent and seasonal, they are important drivers of ocean convection that communicates climate change to the deep ocean.

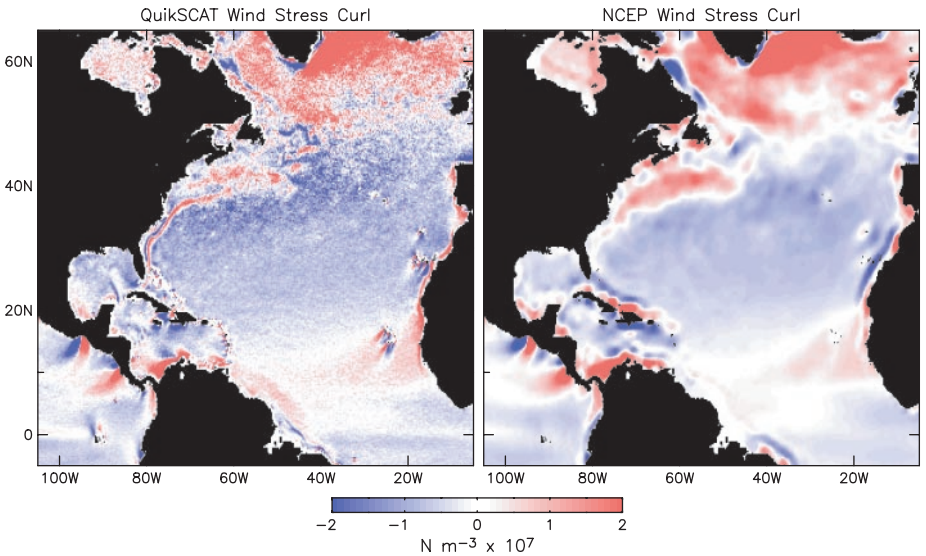

Fig. 2. Four-year averages (August 1999–July 2003) of the curl of the wind stress over the North Atlantic computed from 25-km-resolution wind measurements by the QuikSCAT scatterometer (left) and from the 1° by 1° by 6-hour analyses of winds at 10 m from the U.S. National Centers for Environmental Prediction (NCEP) operational NWP model (right). The alternating positive and negative bands near many of the continental boundaries in the right panel are artifacts of spectral truncation of mountain topography in the spherical harmonic NCEP model (*16*). (See fig. S4 for the 4-year average QuikSCAT and NCEP wind stress curl fields over a larger region that encompasses the North and South Atlantic, the eastern Pacific, and the western Indian Oceans.)

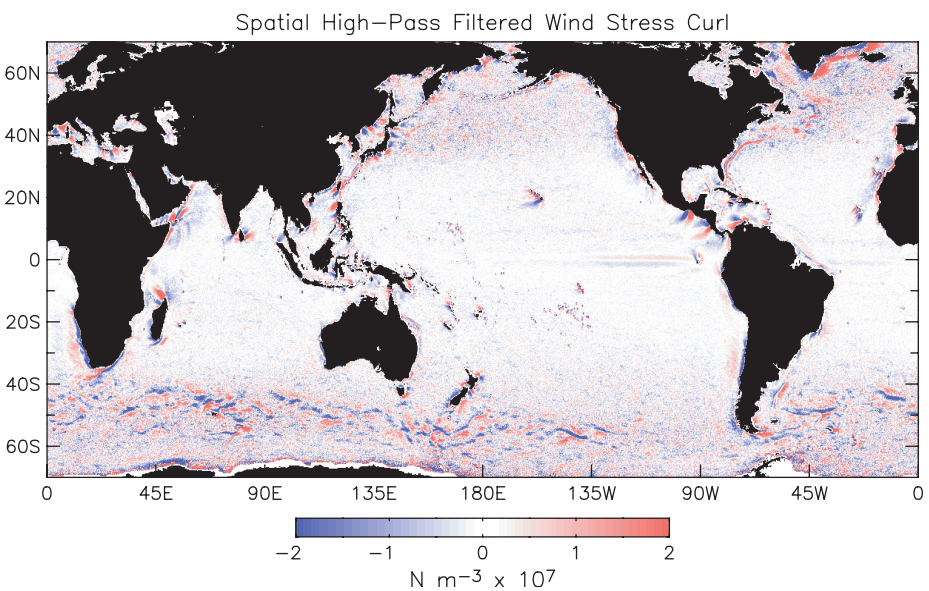

Fig. 3. Global 4-year averages (August 1999–July 2003) of the QuikSCAT wind stress curl shown in the bottom panel of Fig. 1 after spatial high-pass filtering to remove variability with zonal wavelengths longer than 30° of longitude and meridional wavelengths longer than 10° of latitude (*8*). (See fig. S2 for the spatial high-pass–filtered QuikSCAT wind stress divergence and fig. S3 for the spatial high-pass–filtered divergence and curl fields computed from NCEP model winds.)

Another strong corner acceleration is identifiable as a band of negative curl in the lee of the southern tip of Hawaii. This island influence can extend more than 3000 km west of Hawaii during summertime conditions of steady northeast trade winds (*22*). Corner accelerations are also apparent off the southern tip of Madagascar (*35*), the northern tip of the Philippine Island Chain, the southern tip of Tasmania, and numerous tropical islands.

The small patches of alternating positive and negative curl in the lee of the individual Hawaiian Islands are evidence of wind shadows behind each island and wind jets through interisland gaps. Similar features can be seen in Fig. 3 and fig. S2 in the lee of many other islands, including the Cape Verde, Canary, and Madeira Islands in the eastern tropical Atlantic (see also Fig. 2, left), the Galapagos Islands (Fig. 5, top left), Sri Lanka, the northern tip of Madagascar, and numerous small islands throughout the tropics.

Corner accelerations and wind shadows are also prominent in the lee of extratropical islands but are less evident in the 4-year averages considered here because wind direction is much more variable outside of the trade wind regimes. The existence of such features becomes clear when the QuikSCAT data are segregated by averaging the data only during the periods of the prevailing wind direction. The prevailing wind shadows behind the South Georgia and Kerguelen Islands are shown as examples in figs. S7 and S8.

Ocean current effects. The couplet of parallel bands of positive and negative curl that straddle the Gulf Stream along the eastern seaboard of North America (Fig. 5, right) arises because scatterometers measure the actual stress imposed on the sea surface by the wind. This stress depends on the difference between wind and ocean velocities, resulting in significant modification of the stress in regions of strong currents (*36*–*38*). Viewed in the direction of flow, the curl of the velocity field of a narrow ocean current is positive on the left side and negative on the right. Such a current is manifest in reverse in the wind stress curl; negative and positive parallel bands straddle the left and right sides of the current, respectively, opposite the structure of the curl couplet associated with a wind jet.

Although the effects of ocean currents on the wind stress are readily apparent in the curl, ocean current signatures are insignificant in the wind stress divergence because of the quasi-geostrophic and very nearly nondivergent nature of ocean velocity. The bands of relatively weak divergence and convergence associated with the Gulf Stream (top panels of Fig. 1 and figs. S1 and S2) are attributable to the previously discussed SST effects on low-level winds.

SST also affects the wind stress curl over the Gulf Stream, but this is of secondary importance compared with the effects of the current. This becomes apparent by calculating the Gulf Stream contribution to the wind stress curl. Where the Gulf Stream flows north off the Florida coast, the surface ocean velocity can be estimated from QuikSCAT data by assuming that all of the east-west variation of the measured northward wind component is attributable to the effects of ocean velocity on the surface stress. Surface current cross sections calculated in this manner (Fig. 6) compare well with observations (*39*), confirming that the observed wind stress curl couplet is attributable primarily to the surface velocity of the Gulf Stream.

Similar examples of ocean current–induced couplet curl bands in Fig. 3 and fig. S2 include the Loop Current in the Gulf of Mexico (see also Fig. 5, top right), the Labrador Current, the Aleutian Current, the Kuroshio Current in the region between Taiwan and Japan, the Agulhas Current where it separates from the coast of South Africa, the Somali Current northeast of Socotra Island, the Malvinas Current off Argentina, the North Brazil Current, and numerous segments of the ACC.

The curl couplet in the western North Atlantic becomes less well defined after the Gulf Stream separates from the coast at Cape Hatteras, because the broadening of the current and the transient nature of the unstable meanders east of 70°W blur the effects of ocean velocity on the 4-year average wind stress curl. A signature of the Kuroshio Extension east of Japan is similarly blurred by transient meanders that develop after the Kuroshio Current separates from the coast of Japan (*27*). In such regions of meandering currents, the effects of SST become the dominant factor affecting the 4-year average wind stress curl field.

Discussion. High-resolution measurements by the QuikSCAT scatterometer reveal a rich diversity of persistent small-scale features in the global wind stress field that cannot be detected by other means. These features are clear in the 4-year average fields of the wind stress divergence and curl. Small-scale variability is evident in both the divergence and curl in island and coastal regions, where orography influences low-level winds. Over the open ocean, most of the small-scale variability in the divergence field can be attributed to accelerations and decelerations of surface winds blowing across SST fronts owing to SST-induced effects on low-level winds. The resulting convergences and divergences generate vertical motion that can influence atmospheric dynamics and thermodynamics at higher levels in the atmosphere (*40*). SST effects are also manifest in the curl, which is intensified where winds blow parallel to SST fronts.

The high-resolution QuikSCAT data also reveal the surprisingly strong influence of steady ocean currents on the 4-year average wind stress curl field through the relative motion between the ocean currents and the overlying winds. Ocean currents significantly affect the curl on an instantaneous basis wherever they are narrow and intense. Because of the quasi-geostrophic and very nearly nondivergent nature of ocean velocity, ocean currents do not have a significant effect on the wind stress divergence.

An important consideration for ocean circulation modeling is that current-induced features in the wind stress curl are absent in the wind stress fields produced from NWP models (Fig. 2 and figs. S3 and S4). The models estimate the winds relative to fixed locations (the model grid points) and thus effectively consider the ocean surface to be motionless. Because they do not account for the effects of ocean currents on the wind stress, NWP models do not provide the true wind stress that drives the ocean circulation (*36*, *38*).

The importance of ocean current effects on the wind stress depends on the magnitudes and relative directions of the current and wind velocities. For 6 m s^{-1} winds typical of the global open ocean, a moderate surface current of 0.3 m s^{-1} flowing parallel or antiparallel to the wind modifies the wind stress by 10%. In regions of strong currents such as the Gulf Stream and the Kuroshio and Equatorial Current systems, ocean current effects on the wind stress can easily exceed 20%. It is thus clear that oceanic influence on the wind stress is at least regionally important.

Because the existence of persistent small-scale features in the wind field has not heretofore been appreciated, the full implications of these wind patterns for ocean dynamics are only beginning to be explored. The importance of the small-scale variability can be inferred from the zonally integrated wind stress curl across an ocean basin, which provides an approximate estimate of the volume transport of the western boundary currents (*1*). Neglect of small-scale variability can result in underestimates of the volume transports of subtropical western boundary currents by more than 20% (*6*). Stochastic forc-

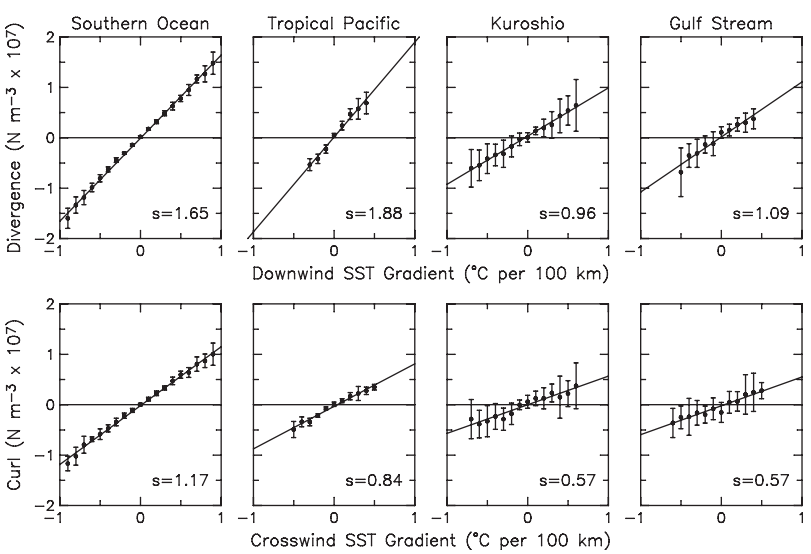

Fig. 4. SST effects on wind stress divergence and curl. Shown are binned scatter plots of spatial high-pass–filtered fields of the wind stress divergence as a function of the downwind SST gradient (top row) and the wind stress curl as a function of the crosswind SST gradient (bottom row) for four geographical regions: the Southern Ocean (60°S to 30°S, 0° to 360°E), the eastern tropical Pacific (5°S to 3°N, 150°W to 100°W), the Kuroshio Extension (32°N to 47°N, 142°E to 170°W), and the Gulf Stream (35°N to 55°N, 60°W to 30°W). The comparisons are based on the first year of satellite SST measurements by the Advanced Microwave Scanning Radiometer (*44*) for the 12-month period from August 2002 to July 2003. The points in each panel are the means within each bin computed from 12 overlapping 6-week averages, and the error bars are the ±1 standard deviation over the 12 samples in each bin. The standard deviations are larger for the Kuroshio and Gulf Stream regions because of seasonal variations in the magnitudes of the divergence and curl perturbations. The coupling between SST and surface winds implied by the slope *s* of the straight line fit by least squares to the binned averages in each panel varies geographically (and seasonally, not shown here), presumably depending on the detailed structure of the MABL, and is consistently larger for the divergence than for the curl (*3*, *4*).

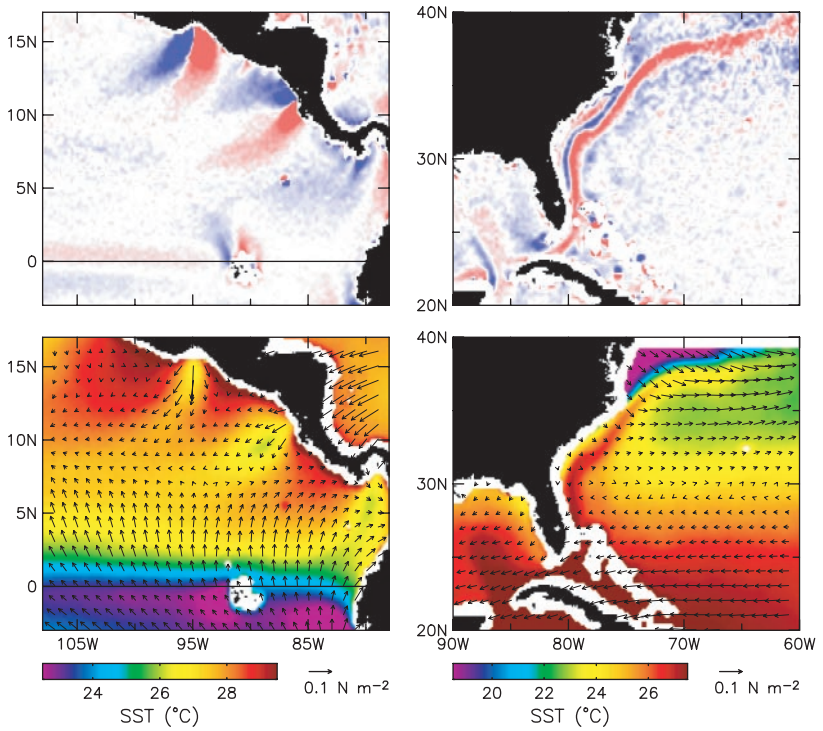

Fig. 5. Four-year averages (August 1999–July 2003) of the spatial high-pass–filtered curl of the wind stress (top) from Fig. 3 and of the SST and vector-average wind stress (bottom) for the eastern tropical North Pacific (left panels) and the western North Atlantic (right panels). The color scale for the wind stress curl is the same as in Figs. 1 to 3. The 4-year average SST fields were derived from satellite measurements by the TRMM (Tropical Rainfall Measuring Mission) Microwave Imager (TMI) (*45*). For clarity, the 25-km wind stress vectors are displayed with reduced resolution on a 1° by 1° grid. The white fringes along the continental margins are gaps in the satellite coverage (about 25 km for QuikSCAT and about 75 km for TMI) owing to land contamination of the microwave signals.

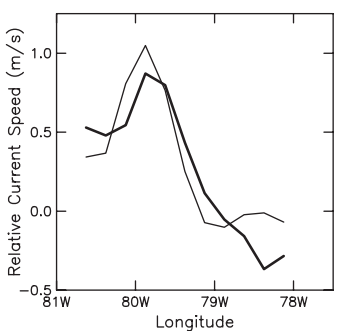

Fig. 6. The 4-year average (August 1999–July 2003) northward surface current velocity across the Gulf Stream at 29.2°N (thin line) and 31.6°N (heavy line) estimated from cross-stream variations in the 4-year average northward component of QuikSCAT wind measurements. The differences between these two surface velocity cross sections separated along-shore by 135 km provide a rough measure of the uncertainty of the calculation. The maximum velocity of about 1 m s^{-1} and the cross-stream width of less than 100 km compare well with observations (*39*) when the 25-km smoothing and 4-year averaging of the QuikSCAT measurements are taken into consideration.

ing by the energetic small-scale variability in the wind stress curl field may also play an important role in the generation of eddies in the open ocean (*41*).

Wind stress curl also generates upwelling and downwelling (*1*) that are important to the dynamics, thermodynamics, and biology of the upper ocean. The vertical velocities associated with the persistent small-scale features that are unresolved by NWP models are comparable in magnitude to the vertical velocities forced by the large-scale wind stress curl (*4*). Because the small-scale variability identified here is present in the 4-year average, there is little doubt that the persistent upwelling associated with these features is important at least locally.

It is also known that air-sea heat fluxes associated with SST-induced variations of surface winds can have a large feedback effect on upper-ocean thermodynamics. In the eastern tropical Pacific, for example, this two-way coupling generates spatial variations of 75 W m^{-2} in the latent heat flux and 15 W m^{-2} in the sensible heat flux (*5*). Comparable SST-induced heat flux variations have been observed south of Africa (*20*). The net air-sea heat flux is further modified by the formation of low-level clouds over warm water from turbulent deepening of the MABL. These clouds reduce the solar radiation incident at the sea surface by 25 W m^{-2} in the equatorial Pacific (*42*).

SST-induced variations in heat fluxes and clouds are also important on the larger scales that are crucial for understanding climate variability. Inadequate representation of these air-sea interaction effects may be one reason that coupled ocean-atmosphere models under development for El Niño research are unable to reproduce the observed structure of the SST patterns in the eastern tropical Pacific (*43*).

The small-scale structures in the global wind stress divergence and curl fields summarized here are statistically robust features in multiyear averages of QuikSCAT measurements. Superimposed on these persistent structures are temporally varying, zero-mean perturbations with magnitudes comparable to the 4-year averages; the small-scale features generally intensify during the winter in mid-latitudes (especially in the Northern Hemisphere) and during the summer and fall in the tropics. The continuing QuikSCAT data record is allowing an improved understanding of the nature of this temporal variability and of the dynamic and thermodynamic impacts of the associated ocean-atmosphere coupling on ocean circulation and atmospheric weather patterns.

References and Notes

1. A. E. Gill, *Atmosphere-Ocean Dynamics* (Academic Press, San Diego, CA, 1982).
2. S.-P. Xie, M. Ishiwatari, H. Hashizume, K. Takeuchi, *Geophys. Res. Lett.* **25**, 3863 (1998).
3. D. B. Chelton *et al.*, *J. Clim.* **14**, 1479 (2001).
4. L. W. O'Neill, D. B. Chelton, S. K. Esbensen, *J. Clim.* **16**, 2340 (2003).
5. N. Thum, S. K. Esbensen, D. B. Chelton, M. J. McPhaden, *J. Clim.* **15**, 3361 (2002).
6. R. F. Milliff, J. Morzel, D. B. Chelton, M. H. Freilich, in preparation.
7. The QuikSCAT scatterometer with its 25-km resolution across a 1600-km swath and 90% global coverage every 24 hours was preceded by scatterometers on the European Space Agency ERS-1 and ERS-2 satellites and by the NASA Scatterometer (NSCAT). The ERS-1 and -2 scatterometers provided a continuous record of wind stress with 70-km resolution from August 1991 through January 2001, but with a 500-km swath width that sampled only 40% of the global ocean in 24 hours. NSCAT provided 50-km-resolution measurements across a 1200-km swath with 75% daily coverage, but operated only for the 9-month period from September 1996 to June 1997.
8. M. G. Schlax, D. B. Chelton, M. H. Freilich, *J. Atmos. Oceanic Technol.* **18**, 1014 (2001).
9. M. H. Freilich, R. S. Dunbar, *J. Geophys. Res.* **104**, 11231 (1999).
10. Scatterometers measure the surface stress. The wind retrievals are calibrated to the equivalent neutral-stability wind at a reference height of 10 m above the sea surface; that is, the wind that would exist if the atmospheric boundary layer were neutrally stratified. The vector wind stress and 10-m neutral-stability wind are simply related by use of a neutral-stability drag coefficient.
11. Because rain tends to occur in cyclonic and convergent conditions, the elimination of rain-contaminated QuikSCAT observations results in large-scale biases in the temporally averaged wind stress derivative fields (*6*). These biases were mitigated here by replacing rain-contaminated data with in-swath smoothed wind stress obtained from a Gaussian-weighted smoother selected to have a wavenumber filter cutoff corresponding to 100 km. This hole filling was applied only if more than 50% of the observations within the span of the smoother were rain-free. The divergence and curl were

then calculated in-swath from the stress components in the hole-filled data set, interpolated to a ¼° grid, and averaged over the 4-year period from August 1999 to July 2003.
12. Because of the complicated space-time sampling pattern of scatterometers, the operations of averaging and differentiation are noncommutative. The swath-by-swath averaging of the curl and divergence fields used here preserves the signals of each individual meteorological event observed by QuikSCAT, thus avoiding first differencing between neighboring grid points composed of averages of the stress components at different observation times.
13. By meteorological convention, winds are referred to by the direction from which they blow.
14. J. P. McCreary, P. K. Kundu, S.-Y. Chao, *J. Mar. Res.* **45**, 1 (1987).
15. A. Bakun, C. S. Nelson, *J. Phys. Oceanogr.* **21**, 1815 (1991).
16. R. F. Milliff, J. Morzel, *J. Atmos. Sci.* **58**, 108 (2001).
17. W. R. Sweet, R. Fett, J. Kerling, P. LaViolette, *Mon. Weather Rev.* **108**, 1042 (1981).
18. J. M. Wallace, T. P. Mitchell, C. Deser, *J. Clim.* **15**, 1492 (1989).
19. S. P. Hayes, M. J. McPhaden, J. M. Wallace, *J. Clim.* **2**, 1500 (1989).
20. M. Rouault, J. R. E. Lutjeharms, *Global Atmos. Ocean Syst.* **7**, 125(2000).
21. H. Hashizume, S.-P. Xie, W. T. Liu, K. Takeuchi, *J. Geophys. Res.* **106**, 10173 (2001).
22. S.-P. Xie, W. T. Liu, Q. Liu, M. Nonaka, *Science* **292**, 2057 (2001).
23. S. P. de Szoeke, C. S. Bretherton, *J. Atmos. Sci.*, in press.
24. M. F. Cronin, S.-P. Xie, H. Hashizume, *J. Clim.* **16**, 3050 (2003).
25. R. J. Small, S.-P. Xie, Y. Wang, *J. Clim.* **16**, 3724 (2003).
26. G. A. Vecchi, S.-P. Xie, A. S. Fischer, *J. Clim.*, in press.
27. M. Nonaka, S.-P. Xie, *J. Clim.* **16**, 1404 (2003).
28. D. B. Chelton, M. H. Freilich, S. K. Esbensen, *Mon. Weather Rev.* **128**, 1993 (2000).
29. E. D. Barton *et al.*, *Oceanography* **6**, 23 (1993).
30. P. C. Fiedler, *Deep-Sea Res.* **49**, 321 (2002).
31. H. Kawamura, P. Wu, *J. Geophys. Res.* **103**, 21,611 (1998).
32. C. Estournel *et al.*, *J. Geophys. Res.* **108**, 8059 (2003).
33. J. D. Doyle, M. A. Shapiro, *Tellus* **51A**, 728 (1999).
34. R. S. Pickart, M. A. Spall, M. H. Ribergaard, G. W. K. Moore, R. F. Milliff, *Nature* **424**, 152 (2003).
35. S. F. DiMarco, P. Chapman, W. D. Nowlin, *Geophys. Res. Lett.* **27**, 3965 (2000).
36. R. C. Pacanowski, *J. Phys. Oceanogr.* **17**, 833 (1987).
37. P. Cornillon, K.-A. Park, *Geophys. Res. Lett.* **28**, 575 (2001).
38. K. A. Kelly, S. Dickinson, M. J. McPhaden, G. C. Johnson, *Geophys. Res. Lett.* **28**, 2469 (2001).
39. E. Johns, D. Wilson, R. L. Molinari, *J. Geophys. Res.* **104**, 25805 (1999).
40. S.-P. Xie, *Bull. Am. Meteorol. Soc.* **85**, 195 (2004).
41. P. Muller, C. Frankignoul, *J. Phys. Oceanogr.* **11**, 287 (1981).
42. C. Deser, J. J. Bates, S. Wahl, *J. Clim.* **6**, 1172 (1993).
43. C. R. Mechoso *et al.*, *Mon. Weather Rev.* **123**, 2825 (1995).
44. F. J. Wentz, T. Meissner, "Algorithm theoretical basis document, Version 2, AMSR Ocean Algorithm" (*Remote Sensing Systems Technical Report RSS 121599A-1*, 2000; available at www.remss.com/papers/AMSR_Ocean_Algorithm_Version_2.doc).
45. F. J. Wentz, C. L. Gentemann, D. Smith, D. B. Chelton, *Science* **288**, 847 (2000).
46. Supported by NASA Ocean Vector Winds Science Team grant NAS6-32965 (D.B.C., M.G.S., and M.H.F.) and by Oregon State University subcontract NS033A-09 (R.F.M.). We thank S. Esbensen, E. Maloney, J. Pullen, S.-P. Xie, J. Small, and J. Achey for helpful comments on the manuscript and B. Vanhoff for data processing support and insightful comments and suggestions throughout the course of this study.

Supporting Online Material
www.sciencemag.org/cgi/content/full/1091901/DC1
Figs. S1 to S8
References

25 September 2003; accepted 23 December 2003
Published online 15 January 2004;
10.1126/science.1091901
Include this information when citing this paper.

Structural Basis of Transcription: An RNA Polymerase II–TFIIB Cocrystal at 4.5 Angstroms

David A. Bushnell, Kenneth D. Westover, Ralph E. Davis, Roger D. Kornberg*

The structure of the general transcription factor IIB (TFIIB) in a complex with RNA polymerase II reveals three features crucial for transcription initiation: an N-terminal zinc ribbon domain of TFIIB that contacts the "dock" domain of the polymerase, near the path of RNA exit from a transcribing enzyme; a "finger" domain of TFIIB that is inserted into the polymerase active center; and a C-terminal domain, whose interaction with both the polymerase and with a TATA box–binding protein (TBP)–promoter DNA complex orients the DNA for unwinding and transcription. TFIIB stabilizes an early initiation complex, containing an incomplete RNA-DNA hybrid region. It may interact with the template strand, which sets the location of the transcription start site, and may interfere with RNA exit, which leads to abortive initiation or promoter escape. The trajectory of promoter DNA determined by the C-terminal domain of TFIIB traverses sites of interaction with TFIIE, TFIIF, and TFIIH, serving to define their roles in the transcription initiation process.

RNA polymerase II (pol II) assembles with five general transcription factors and Mediator at every promoter before the initiation of transcription (Table 1). This giant complex of 50 or more polypeptides, with a total mass in excess of 2.5 million daltons, recognizes promoter DNA, responds to regulatory information, and synthesizes the first dozen residues of the RNA transcript. Elucidation of the structure and mechanism of the initiation complex is necessary for understanding transcriptional regulation. We took a first step in this direction with the x-ray structure determination of pol II, itself a complex of 12 polypeptides and mass of 0.5 MD (*1*–*4*). We also determined the structure of pol II in the act of transcription, revealing the template unwound in a "transcription bubble" and the transcript in an RNA-DNA hybrid (*5*). We now report the structure of a cocrystal of pol II with general transcription factor IIB (TFIIB), the critical component for both assembly and disassembly of the transcription initiation complex.

TFIIB and TFIID are responsible for promoter recognition and interaction with pol II; together with pol II, they form a minimal initiation complex, capable of transcription under certain conditions (see below). The TATA box of a pol II promoter is bound in the initiation complex by the TBP subunit of TFIID, which bends the DNA around the C-terminal domain of TFIIB ($TFIIB_C$). The N-terminal domain of TFIIB ($TFIIB_N$) interacts with pol II (*6*, *7*). The first evidence for a role of TFIIB in "bridging" between promoter DNA and pol II came from binding studies, which showed a requirement for TFIIB for interaction of a TBP-promoter DNA complex with pol II (*8*). The functional relevance of this interaction was demonstrated by transcription with purified proteins from budding

Table 1. RNA polymerase II transcription machines. Mass data are for yeast proteins. Details about function are in the text. TAF, TBP-associated factor.

Component	Subunits	Mass (kD)	Function
Pol II	12	520	RNA synthesis
TFIIB	1	38	Start site determination
TFIID (TBP)	1	27	Bending TATA box DNA around TFIIB and pol II
(TAFs)	14	749	Promoter recognition
TFIIE	2	92	Coupling pol II–promoter interaction to recruitment of TFIIH
TFIIF	3	156	Interaction with nontemplate DNA strand
TFIIH	9	525	Promoter opening, pol II phosphorylation
Mediator	20	1003	Regulatory signal transduction

Department of Structural Biology, Stanford University School of Medicine, Stanford, CA 94305–5126, USA.

*To whom correspondence should be addressed. E-mail: kornberg@stanford.edu.